A Comparative Study on Ground Coil Start-Up Current Control Methods for Dynamic Wireless Power Transfer Systems

Binh-Minh Nguyen*, Ryo Matsumoto, Toshiyuki Fujita, Osamu Shimizu, Hiroshi Fujimoto

（The University of Tokyo）

This paper compares several methods for ground coil current control in dynamic wireless power transfer. Simulation and experimental results show that the super-twisting-algorithm based PI controller performs better than the traditional PI controller in terms of overshoot suppression, especially when the mutual inductance varies from a very small value.

Keywords: current control, dynamics wireless power transfer (DWPT), super-twisting algorithm (STA), mutual inductance, overshoot, sliding mode control (SMC).

1. Introduction

Dynamic wireless power transfer (DWPT) using magnetic resonance coupling has been recognized as one of the promising technologies toward transportation electrification [1]. Fig. 1 demonstrates a DWPT experimental system developed at our research group. This technology raises many new research topics, such as start-up time determination [2], misalignment estimation using power information [3], [4], metal object detection [5], [6], economic viability and environmental impact [7].

To realize DWPT, one of the most challenges is power fluctuations due to coil misalignment and circuit parameter uncertainties. Especially, the relative position between the coils changes continuously during the charging. Thus, stably controlling the current even with small mutual inductance in a short period becomes a nontrivial question. Furthermore, it is required to quickly suppress the current overshoot at the start-up moment. To this end, many previous studies have focused on the start of power transmission by primary side current control [8] – [13]. For instance, [8] experimentally verified that the proposed controller is robust to a sharp change of 50% in coupling coefficient. Unfortunately, almost of the previous studies merely utilized the proportional-integral (PI) controller without considering system stability analysis. To this end, we established in [13] a circle criterion that guarantees the absolute stability of the DWPT system as the mutual inductance varies between a lower-bound and an upper-bound. However, to the best of our knowledge, there exists no comparative study on the startup current control.

With respect to the above discussion, this paper aims to provide a comparative study of several current feedback control methods.
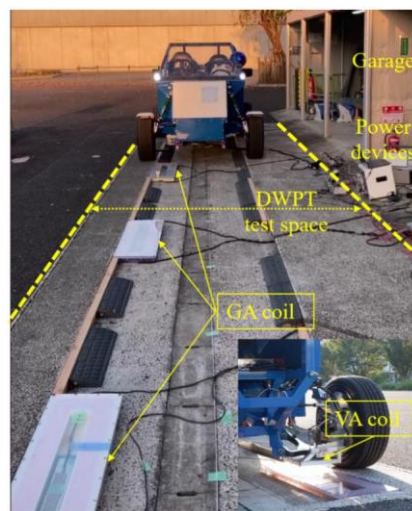

Fig. 1. DWPT test at the authors' research group [4].

To this end, this paper focuses on the DWPT system with the S-S topology. Three methods were implemented and evaluated by both simulation and experiments: (1) PI controller, (2) PI controller with lead compensator, and (3) super twisting sliding mode control (ST-SMC) [14]. The controllers (1) and (2) were designed using the circle-criterion-based procedure [13]. Both simulation and experiment were conducted. Test results show that the PI with lead compensator can slightly reduce the current overshoot. Notably, the ST-SMC allows the non-overshoot startup current, even with a very small mutual inductance.

The reminder of this paper is organized as follows. Section 2 presents the envelope model for current control design. Section 3 presents the design of the aforementioned methods. Simulation and experimental results are shown in Sections 4 and 5, respectively. Finally, the conclusions are stated in Section 6.

2. Envelop current model

This study considers the DWPT system with an S-S equivalent circuit model shown in Fig. 2, and the main parameters are defined in Table 1. The capacitors are designed to satisfy the resonance condition $\omega_o^2 L_1 C_1 = \omega_o^2 L_2 C_2 = 1$. With respect to the bandpass characteristics of the DWPT circuit, the currents are sine waves at the resonant frequency. Therefore, it is possible to focus on the fundamental amplitudes of the voltage $v_1(t)$ and current waveforms $i_1(t)$ and $i_2(t)$. They are denoted as $V_1(t)$, $I_1(t)$ and $I_2(t)$, respectively. We have:

$$v_1 = V_1 \sin(\omega_o t), I_1 = I_1 \sin(\omega_o t), I_2 = I_2 \cos(\omega_o t) \quad \ldots\ldots(1)$$

As shown in Table 1, ω_o is commonly a very big value in DWPT system. Thus, by neglecting the small terms of high orders, the following approximations can be derived [13].

$$\frac{1}{C_1} \int i_1 dt = \frac{1}{C_1} \int I_1 \sin(\omega_o t) dt$$

$$= \frac{-1}{\omega_o C_1} \left(I_1 \cos(\omega_o t) - \int \frac{dI_1}{dt} \cos(\omega_o t) dt \right) \quad \ldots\ldots\ldots\ldots(2)$$

$$\approx \frac{-1}{\omega_o C_1} I_1 \cos(\omega_o t) + \frac{1}{\omega_o^2 C_1} \frac{dI_1}{dt} \sin(\omega_o t)$$

$$M \frac{di_2}{dt} = M \left(\frac{dI_2}{dt} \cos(\omega_o t) - \omega_o I_2 \sin(\omega_o t) \right) \quad \ldots\ldots\ldots\ldots(3)$$

$$\approx -\omega_o M I_2 \sin(\omega_o t)$$

Substitute (1), (2) and (3) into the Kirchhoff's voltage equations of Fig. 2 at a given value of the mutual inductance, and then applying the Laplace transformation, the transfer function from V_1 to I_1 can be established as:

$$G(s) = \frac{\dfrac{1}{2L_1} s + \dfrac{R_L}{4L_1 L_2}}{s^2 + \dfrac{R_L}{2L_2} s + \dfrac{(\omega M)^2}{4L_1 L_2}} = \frac{\beta_1 s + \beta_0}{s^2 + \alpha_1 s + \alpha_0} \quad \ldots\ldots\ldots(4)$$

3. Candidates for primary side current control

⟨3·1⟩ **Method 1 (PI controller)** The current control system is shown in Fig. 3(a) where I_1^* is the reference value and $C_1(s) = (K_{p1}s + K_{i1})/s$ is the transfer function of the PI controller. From (44), the system in Fig. 3(a) can be equivalently expressed as the system in Fig. 3(b) and Fig. 3(c) where:

$$P_1(s) = \frac{\beta_1 s + \beta_0}{s^2 + \alpha_1 s}, \ P_2(s) = \frac{\gamma}{s^2 + \alpha_1 s}, \ \gamma = \frac{1}{4L_1 L_2} \quad \ldots\ldots\ldots(5)$$

$$H_1(s) = \frac{P_2(s)}{1 + C_1(s) P_1(s)}, \ \varphi(t) = \omega^2 M^2 \quad \ldots\ldots\ldots\ldots(6)$$

$\varphi(t)$ varies between a lower-bound $\underline{\varphi} = \omega^2 M_{min}^2$ and an upper-bound $\overline{\varphi} = \omega^2 M_{max}^2$. According to the circle criterion [15],
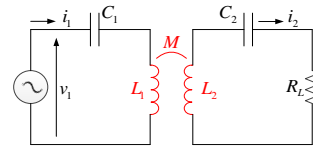

Fig. 2. DWPT circuit model.

Table 1. Parameters of DWPT system used in this study.

Parameter	Meaning	Value
L_1	Primary coil inductance	$246 \ \mu H$
L_2	Secondary coil inductance	$106 \ \mu H$
C_1	Primary capacitor	$14.2 \ nF$
C_2	Secondary capacitor	$33.7 \ nF$
R_L	Load resistance	$5.7 \ \Omega$
ω_o	Resonant frequency	$2\pi \times 85000 \ rad/s$
M_{min}	Minimum mutual inductance	$4 \ \mu H$
M_{max}	Maximum mutual inductance	$20 \ \mu H$
$V_{1,max}$	Maximum voltage of inverter	$30 \ V$
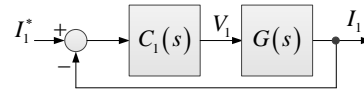
(a) Original control system.
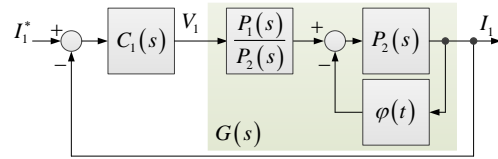
(b) Equivalent block diagram.
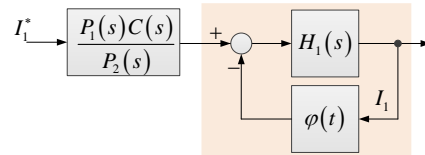
(c) Equivalent diagram for system analysis.
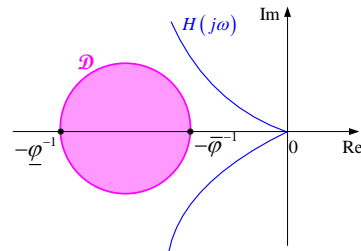
Fig. 3. Current control system using PI controller.

Fig. 4. Definition of disk $\mathcal{D}$.

the current control system in Fig. 3 is absolutely stable if the Nyquist plot of $H_1(j\omega)$ does not enter disk $\mathcal{D}$ defined by $\underline{\varphi}$ and $\overline{\varphi}$ in Fig. 4. Thus, the PI controller is designed by assigning stable poles to $H_1(s)$ such that the absolute stability condition is satisfied. A procedure to design and adjust the PI gains can be found in our recent study [13].

⟨3·2⟩ **Method 2 (PI controller with compensator)** To enhance the performance of the PI controller, an idea is to combine it with a lead compensator. This means the PI controller in Fig. 3 can be replaced by:

$$C_2(s) = \frac{K_{p2}s + K_{i2}}{s} \frac{T_2s + 1}{\alpha_2 T_2 s + 1}, \ 0 < \alpha_2 < 1 \ ....(7)$$

The lead compensator improves the phase margin, thereby reducing the overshoot of the system [16]. The trade-off is that the lead compensator increases the high frequency gain of the system, which makes the system more susceptible to noise. This trade-off should be considered when designing the controller gains of $C_2(s)$. The design procedure for $C_2(s)$ is similar to that of $C_1(s)$. The control parameters $\{K_{p2}, K_{i2}, \alpha_2, T_2\}$ are determined by pole placement to the transfer function

$$H_2(s) = \frac{P_2(s)}{1 + C_2(s)P_1(s)}$$

such that the Nyquist plot of $H_2(j\omega)$ does not enter disk $\mathcal{D}$ defined by $\underline{\varphi}$ and $\overline{\varphi}$ in Fig. 4.

⟨3·3⟩ **Method 3 (ST-SMC or PI-like-SMC)** The current control system with ST-SMC is shown in Fig. 5. The ST-SMC is a nonlinear proportional integral like sliding mode controller which is implemented based on super-twisting algorithm (STA) [14]. The STA allows us to realize a second order sliding mode. Moreover, it is able to compensate for a Lipschitz disturbance theoretically exactly and provide the finite-time convergence for output variable and its derivative. As shown in Fig. 5, the voltage command of the primary side inverter is calculated as follows with $e = -(I_1^* - I_1)$:

$$V_1 = -K_{p3} sqrt(abs(e))sign(e) - \frac{K_{i3}}{s} sign(e) \ ....(8)$$

where $sqrt()$ and $abs()$ are the functions that calculate the square root and absolute value of the number e; and $sign()$ is the signum function.

For the sake of practical application, the control gains $\{K_{p3}, K_{i3}\}$ are adjusted with respect to the following remarks.

Remark 1: At the start-up moment, the mutual inductance M is very small. Therefore, we can assume that $\alpha_0 \approx 0$ in the transfer function $G(s)$. Since $\beta_0 = \beta_1\alpha_1$, it is possible to approximate the transfer function from V_1 to I_1 by a nominal transfer function:

$$G_n(s) = \frac{\beta_1 s + \beta_0}{s^2 + \alpha_1 s + 0} = \frac{\beta_1 s + \beta_1\alpha_1}{s^2 + \alpha_1 s} = \frac{\beta_1}{s} \ ....(9)$$

Consequently, the nominal dynamics of the primary side current can be expressed as:

$$\dot{I}_1 = \beta_1 V_1 + f_d = \tilde{V}_1 + f_d \ ....(10)$$
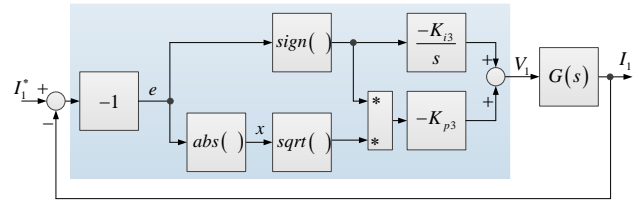

Fig. 5. Current control system using ST-SMC.

where the term f_d represents the lumped disturbance, which includes the real disturbance to the system and the mismatch between the nominal dynamics model (9) and the real dynamics model (4). Assuming that f_d is Lipschitz, such as $|\dot{f}_d| < \delta$, where δ is a constant. The necessary and sufficient stability condition for the closed-loop nominal system is as follows [14]:

$$K_{i3} > \delta, \ K_{p3} > \sqrt{\delta + K_{i3}} \ ....(11)$$

Let δ be a tuning parameter, the gains $\{K_{p3}, K_{i3}\}$ can be obtained after a fine-tuning process.

Remark 2: To rigorously derive the stability condition for the control system in Fig. 5, it is possible to apply the Describing Function (DF) approach to the transfer function $G(s)$ in (4) to establish a Harmonic Balance equation $N(A, w)G(jw) = -1$, where $N(A, w)$ is the DF for STA. The solution of this equation is the amplitude A and frequency w of the sliding mode's chattering phenomenon. Then, system stability can be discussed via the Loeb's criterion of orbital stability of periodic motions [17].
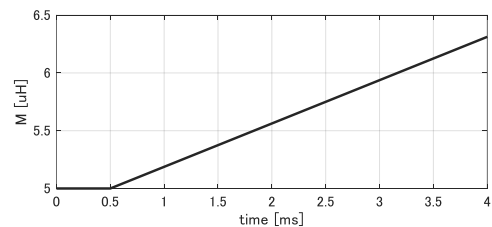

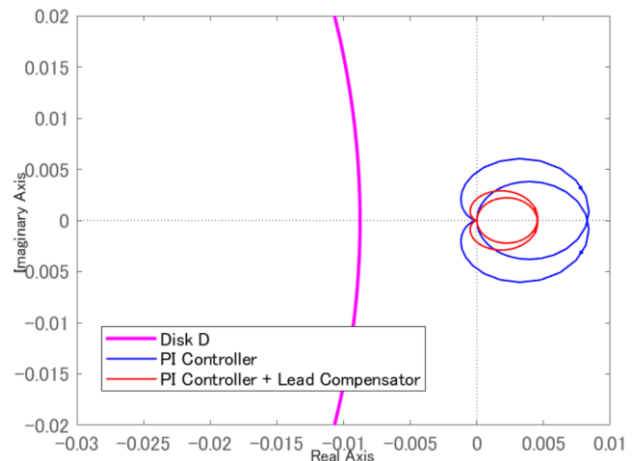Fig. 6. Mutual inductance in the simulation.

Fig. 7. Circle criterion test of Method 1 and Method 2.

4. Simulation evaluation

⟨4·1⟩ **Simulation setting** By using the parameters in Table 1, a simulator of the DWPT system was established using MATLAB R2024a. At the start-up moment, the mutual inductance increases from a small value of $5\ \mu H$, as shown in Fig. 6. The current reference is set to be $I_1^* = 1.5\ A$, and the start-up moment is at 0.5 millisecond. Utilzing the design approaches described in the previous Section, the control gains of three methods were selected as follows:

- Method 1: $K_{p1} = 17.7,\ K_{i1} = 1.59 \times 10^5$
- Method 2: $K_{p2} = 17.7,\ K_{i2} = 1.59 \times 10^5$,
  $$T_2 = 0.0002[s],\ \alpha_2 = 0.5$$
- Method 3: $K_{p3} = 17.8,\ K_{i3} = 8.1$

In detail, the PI gains of Method 1 are obtained by placing the one pole of $H_1(s)$ at $-\alpha_1$ and other two poles at -1.8×10^4. The absolute stability of the control system with Methods 1 and 2 is clarified by the circle criterion test in Fig. 7. It can be seen that the Nyquist plots do not enter the disk $\mathcal{D}$ for both methods. Besides, the gains of the ST-SMC were obtained under the assumption that the volume of $\dot{f}_d$ is bounded by $\delta = 8$.

⟨4·2⟩ **Simulation result** As can be seen in Fig. 8, by adding the Lead Compensator, Method 2 can reduce the current overshoot in comparison with Method 1. Furthermore, the current overshoot is eliminated by Method 3, thanks to the STA sliding mode control. The root-mean-square-deviation (RMSE) values of Methods 1, 2 and 3 are $0.1165\ A$, $0.1007\ A$, and $0.0338\ A$, respectively. In other words, the STA algorithm reduces the current tracking error by 70% in comparison to the PI algorithm.

However, there exists a trade-off between current tracking performance and the chattering of the inverter voltage. As shown in Fig. 8(d), the inverter voltage fluctuates at high frequency when utilizing Method 3.

5. Experimental evaluation

⟨5·1⟩ **Experiment setting** To conduct the experiment, we used the test-bench shown in Fig. 9. The parameters of the DWPT circuit are summarized as in Table 1. This test-bench can adjust the relative position between the primary coil and secondary coil. An FPGA board is used to obtain the envelope of the current in real-time. We used a digital control system PE-Expert4, which was provided by Myway Plus Corporation. This control system is to perform different control algorithms, display the result in real-time, and store the experimental data. In addition to using a high-performance DSP, communication times and delays have been reduced, dramatically improving processing speed.
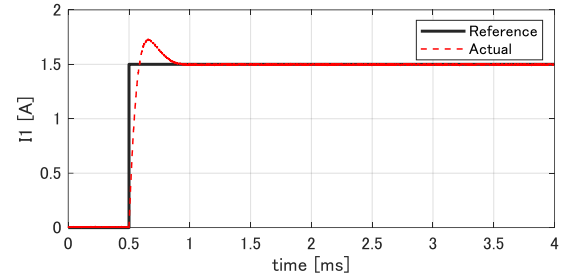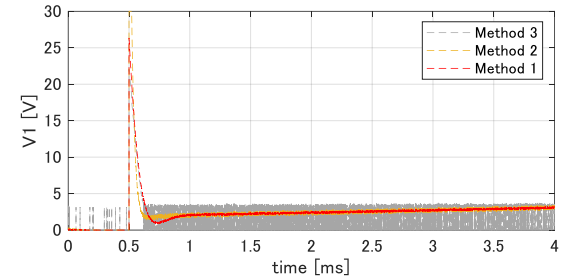

(a) Method 1: PI Controller.
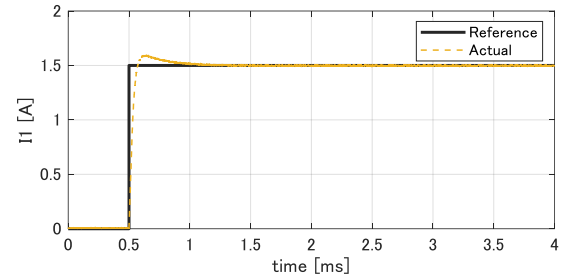
(b) Method 2: PI Controller with Lead Compensator.
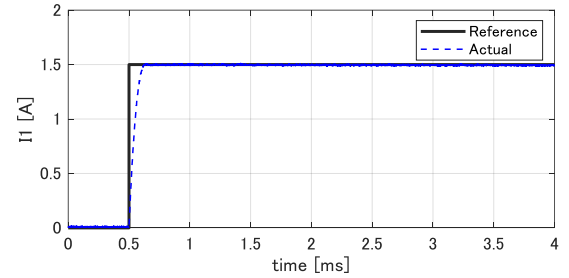

(c) Method 3: ST-SMC.

(d) Primary side inverter voltage.

Fig. 8. Simulation results.

General vector control processing, including PWM command output, can be completed in $5\ \mu s$ or less. The control algorithms were implemented using C programming. The oscilloscope produced by Tektronix is used to measure the voltage and current waveforms. The start-up moment suffers very large misalignments between two coils: The longitudinal and lateral misalignments are $450\ mm$ and $60\ mm$, respectively, while the airgap is fixed at $85\ mm$. With this setting, the star-tup mutual inductance is about $5\ \mu H$, which is similar to the simulation.
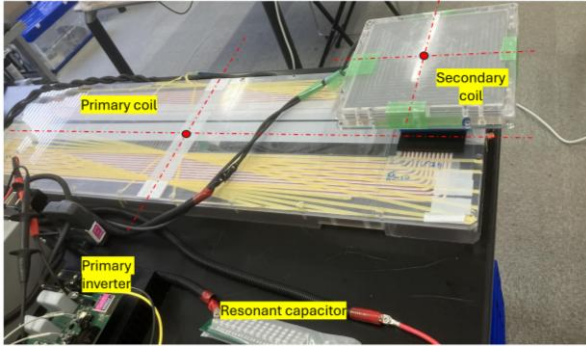
(a) Coil setting for start-up current control.
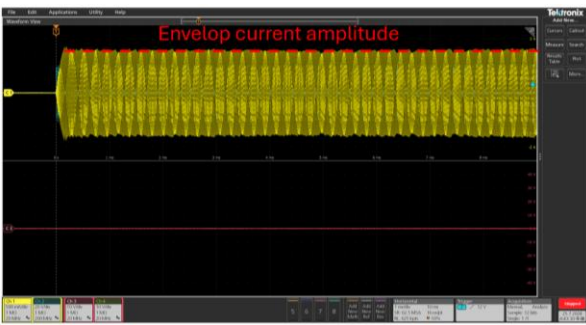
(b) Current waveform on oscilloscope screen.
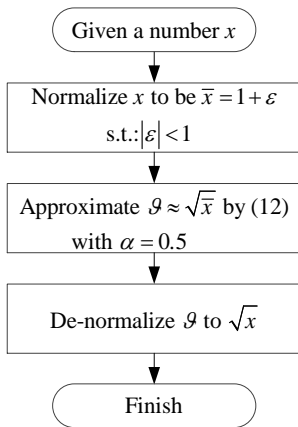
Fig. 9. Test-bench system.

Fig. 10. Approximation of the square-root.

⟨5·2⟩　　　**STA implementation**　　　PE-Expert 4 is not provided with the fractional order function in its C program library. Therefore, it is impossible to calculate the square root of a number directly. To realize the ST-SMC algorithm (8), we will approximate the square root function by binomial series expansion (Taylor series). Let $\bar{x} = 1 + \varepsilon$ where $|\varepsilon| < 1$, we have:

$$\bar{x}^{\alpha} = \lim_{N \to \infty} \sum_{n=0}^{N} \left[\frac{\alpha(\alpha-1)\cdots(\alpha-n+1)}{n!} x^n \right] = \vartheta \quad \ldots\ldots\ldots (12)$$

Fig. 10 describes a procedure to approximately calculate the square root by using C programming. The normalization is
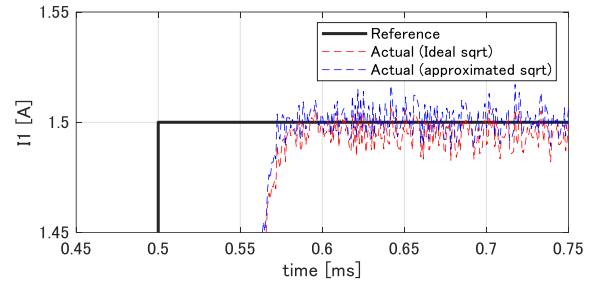

Fig. 11. Simulation of ST-SMC with ideal sqrt function and with the approximation procedure in Fig. 10.

performed as $\bar{x} = x/A$ where A is a big enough number such that: (i) Its square root is understandable (i.e., $A = 25$, 100, $400...$); (ii) $|x/A - 1| < 1$. Thus, the de-normalization step can be performed by multiplying with the square root of A.

To evaluate the proposed procedure, we repeated the simulation of Method 3 in the previous Section by two cases: Case 1: The square root is ideally calculated using MATLAB's function sqrt. Case 2: The square root is approximately calculated using the procedure in Fig. 10 with $N = 10$ and $A = 100$. The results in Fig. 11 shows that the binomial series expansion successfully approximates the square root for realizing the ST-SMC in real time.
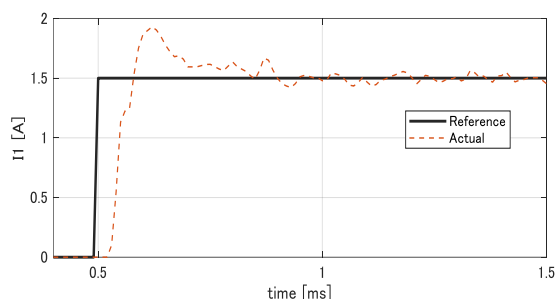
⟨5·3⟩　　　**Experiment results**　　　The experiment results of three methods are shown in Fig. 12. Transparently, Method 1 has the highest overshoot. By adding the Lead Compensator, Method 2 attains better performance in comparison with Method 1. By using the super twisting algorithm, Method 3 can control the current without overshoot. This is the same as the conclusion of the simulation.

The RMSE values of Methods 1, 2 and 3 are $0.3222\,A$, $0.2481\,A$, and $0.2106\,A$, respectively. These values are bigger than the RMSE values of the simulation. This can be explained due to the influence of sensor noises and a small delay-time for measurement communication and signal processing.

6. Conclusions

This paper provides a thorough comparison of three candidates for the primary side current control in DWPT system. Both simulation and experiment clarify that the start-up current overshoot can be reduced by adding the lead compensator to the PI controller, or by utilizing the ST-SMC. In addition, the STA algorithm is shown to be effectively implemented using binomial series expansion. Future study will consider the chattering analysis of the ST-SMC with respect to model uncertainty and measurement delay. To compromise the trade-off between overshoot reduction and voltage chattering, it is possible to examine a current control switching strategy: ST-SMC in the start-up moment, and PI controller as the current reaches the steady state.

(a) Method 1: PI Controller.
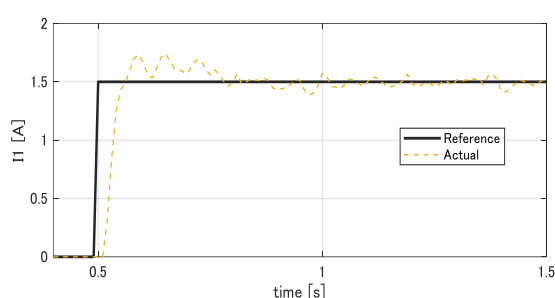
(b) Method 2: PI Controller with Lead Compensator.
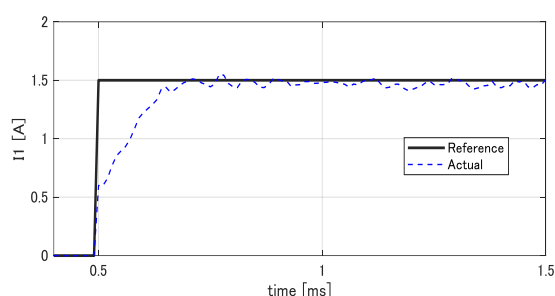
(c) Method 3: ST-SMC.

Fig. 12. Experiment results.

Acknowledgements

References

(1) T. Newbolt, P. Mandal, H. Wang and R. Zane, "Sustainability of Dynamic Wireless Power Transfer Roadway for In-Motion Electric Vehicle Charging," IEEE Transactions on Transportation Electrification, Vol. 10, No. 1, pp. 1347-1362, 2024.

(2) T. Hamada, D. Shirasaki, T. Fujita and H. Fujimoto, "Proposal of Sensorless Vehicle Detection Method for Start-up Current Control in Dynamic Wireless Power Transfer System," 47th Annual Conference of the IEEE Industrial Electronics Society, pp. 1-6, 2021.

(3) R. Tavakoli, T. Shabanian, E. M. Dede, C. Chou and Z. Pantic, "EV Misalignment Estimation in DWPT Systems Utilizing the Roadside Charging Pads," IEEE Transactions on Transportation Electrification, Vol. 8, No. 1, pp. 752-766, 2022.

(4) T. Koishi, B. -M. Nguyen, O. Shimizu and H. Fujimoto, "Receiving Side Current-Based Lateral Misalignment Estimation and Automated Steering Control for Dynamic Wireless Power Transfer," IEEE Journal of Emerging and Selected Topics in Industrial Electronics, 2024.

(5) B. Long, Q. Zhu, S. Zang, L. Zhao and A. P. Hu, "Metal Object Detection by Monitoring Fifth-Order Harmonic Current of IPT System with Dual Frequency Tuning," IEEE Transactions on Power Electronics, Vol. 37, No. 3, pp. 2513-2518, 2022.

(6) W. Zhong, F. Xiang and C. Hu, "Metal Object Detection with Detection Coils Perpendicular to Power Coils for Wireless Power Transfer Systems," in IEEE Transactions on Power Electronics, Vol. 38, No. 9, pp. 10530-10534, 2023.

(7) B. J. Limb et al., "Economic Viability and Environmental Impact of In-Motion Wireless Power Transfer," IEEE Transactions on Transportation Electrification, Vol. 5, No. 1, pp. 135-146, 2019.

(8) J. Jiang, K. Song, Z. Li, C. Zhu, and Q. Zhang, "System Modeling and Switching Control Strategy of Wireless Power Transfer System," IEEE Journal of Emerging and Selected Topics in Power Electronics, Vol. 6, No. 3, pp. 1295-1305, 2018.

(9) W. Shi, J. Deng, Z. Wang, and X. Cheng, "The Start-up Dynamic Analysis and One Cycle Control-PD Control Combined Strategy for Primary-Side Controlled Wireless Power Transfer System," IEEE Access, Vol. 6, pp. 14439-14450, 2018.

(10) J. Noeren and N. Parspour, "Model Predictive Control for Contactless Energy Transfer Systems," IEEE PELS Workshop on Emerging Technologies: Wireless Power Transfer, pp. 6-9, 2020.

(11) K. Hata, T. Imura, H. Fujimoto, and Y. Hori, "Soft-Start Control Method for In-motion Charging of Electric Vehicles Based on Transient Analysis of Wireless Power Transfer System," IEEE Energy Conversion Congress and Exposition, pp. 2009-2015, 2018.

(12) G. Guidi, J. A. Suul, and H. Fujimoto, "Conditions for Maximum Energy Transfer in Inductive Road-Powered Electric Vehicle Applications Taking System Limitation into Account," 5th International Electric Vehicle Technology Conference, 2021.

(13) B.-M. Nguyen, R. Matsumoto, M. Mae, T. Fujita, and H. Fujimoto, "Basic Study on Ground Coil Current Control for WPT with the Consideration of Time-Varying Mutual-Inductance," Joint Technical Meeting on Semiconductor Power Converter, Home and Consumer Appliances, and Vehicle Technology, IEE Japan, 2023.

(14) M. A. Estrada, M. Ruderman, L. M. Fridman, "Super-twisting based Sliding Mode Control of Hydraulic Actuator without Velocity State," Control Engineering Practice, Vol. 142, 105739, 2024.

(15) H. Khalil, "Nonlinear Systems," Prentice Hall, 2002.

(16) K. Ogata, "Modern Control Engineering," 5th Edition, Pearson, Upper Saddle River, 2005.

(17) U. Perez-Ventura and L. Fridman, "Design of Super-twisting Control Gains: A Describing Function Based Methodology," Automatica, Vol. 99, pp. 175-180, 2019.